Eng. Sci., 2025, **38**, 1904

Engineered Science
DOI: https://dx.doi.org/10.30919/es1904

Catalytic Performance of ZrCu Bimetal Supported MCM-41 in the Pyrolysis of Oleic Acid for C_8-C_{17} Aviation-Grade Biofuels

Chunxia Song,[1,2] Kai Zhang,[1,2] Naidong Li,[1,2] Xiaoqing Yan,[1,2] Fashe Li,[3] Xianghong Li[1,2,*] and Juan Xu[1,2,*]

Abstract

With global energy consumption rising and fossil fuel reserves depleting, biofuels are becoming significant as renewable energy sources. Oleic acid in vegetable oils is vital for catalytic cracking to produce hydrocarbon-rich biofuels, to replace conventional petroleum resources. However, oxygenated compounds in direct pyrolysis products restrict their direct use as transportation fuels, so efficient catalytic systems are required. In this research, a ZrCu bimetallic catalyst supported on mesoporous MCM-41 (xZr-yCu/MCM-41) was synthesized by incipient wetness impregnation. The structural properties were characterized by techniques such as XRD, FT-IR, N_2 adsorption-desorption, and NH_3-TPD. The 2Zr-Cu/MCM-41 catalyst had the best activity. At 500 °C, an alcohol-to-oil ratio of 5:1, and a 1 g catalyst dosage, oleic acid conversion reached 100%, with 90.6% hydrocarbon selectivity and 76.7% hydrocarbon yield in the C_8-C_{17} aviation fuel range. The Zr-Cu alloy phase optimized acidic site distribution (Zr for deoxygenation, Cu for hydrogenation). The mesoporous MCM-41 (3.8 nm average pore diameter) enhanced mass transfer and active site exposure. The catalyst maintained stable performance after three cycles, with coke resistance and thermal stability due to metal-support interactions. This study provides theoretical and experimental insights for biomass conversion bimetallic catalytic system design.

Keywords: ZrCu bimetallic/MCM-41 catalyst; Oleic acid pyrolysis; Aviation biofuel; C_8-C_{17} hydrocarbons.
Received: 25 September 2025; Revised: 19 November 2025; Accepted: 25 November 2025
Article Type: Research article.

1. Introduction

With the rapid growth of global energy demand and the gradual depletion of fossil fuel resources, biofuels have emerged as a crucial renewable energy source and attracted extensive attention.[1] Among various biomass conversion technologies, pyrolysis is an effective approach to convert biomass into high-value liquid fuels and chemicals.[2] Oleic acid, a monounsaturated fatty acid commonly present in vegetable oils, is regarded as an excellent feedstock for bio-oil conversion. Through catalytic cracking, oleic acid can be transformed into hydrocarbon-rich biofuels, which are of great significance for substituting traditional petroleum resources.[3] However, direct pyrolysis of biomass typically produces complex mixtures with high concentrations of oxygenated compounds. These compounds exhibit poor thermal stability, low energy density, and tend to corrode engine components,[4-6] severely restricting their direct use as transportation fuels. Therefore, developing efficient catalytic systems to upgrade biomass pyrolysis products into hydrocarbon-rich biofuels possesses substantial scientific and practical significance.

Enhancing the activity, selectivity, and cycle stability of catalysts remains as a key challenge in the catalytic cracking process of oleic acid.[7] Although single-metal catalysts and ordered mesoporous materials have been extensively studied, they often suffer from limitations such as single active sites and insufficient selectivity during product upgrading.[8] These drawbacks make it difficult to achieve both efficient deoxygenation and precise carbon-chain regulation, resulting in broad product distributions and low yields of target products. Moreover, numerous studies have focused on the synergistic effects between single-metal components and their supports, while often overlook the potential synergies between metals and the porous structures,[9] which restricts the catalytic efficiency and product distribution in the catalytic cracking process.[10]

MCM-41 is an ordered silica-based molecular sieve with a two-dimensional cubic structure. Its well-defined framework, determined by the orientation of expanded pores, endows it with a high specific surface area and narrow pore size distribution.[11] Due to its large specific surface area and pore

[1]*Key Laboratory of State Forestry and Grassland Administration on Highly-efficient Utilization of Forestry Biomass Resources in Southwest China, Southwest Forestry University, Kunming, Yunnan, 650224, China*
[2]*College of Materials and Chemical Engineering, Southwest Forestry University, Kunming, 650224, China*

volume, MCM-41 provides an excellent platform for the dispersion of metal active centers, making it highly suitable for adsorption and catalytic applications. Zirconium (Zr) and copper (Cu), as cost-effective alternatives to noble metals, have garnered significant attention in catalytic hydrogenation processes due to their low cost and efficient catalytic performance. Particularly, zirconia exhibits both acidic and basic sites on its surface, which are advantageous for catalytic cracking reactions. Ma *et al*.[12] reported the application of Zr-based catalysts in the upgrading of pyrolysis oil, indicating that the acidic sites of Zr can effectively facilitate the deoxidation of oxygen-containing compounds, leading to the production of light olefins and aromatics. Nevertheless, this study primarily concentrated on the acidic properties of Zr and did not fully exploit the hydrogenation capabilities of metals, thereby restricting the control over product distribution.

Copper-based catalysts are widely used in the chemical industry due to their excellent catalytic properties in hydrogenation, dehydrogenation, and oxidation reactions. They find applications in methanol steam reforming, CO oxidation, methanol synthesis, dimethyl oxalate hydrogenation to ethylene glycol, and hydrodeoxygenation.[13-15] Li *et al*.[16] demonstrated that Cu can facilitate the hydrogenation of unsaturated compounds to form corresponding alkanes. Nevertheless, Cu-based catalysts exhibit relatively low activity in deoxygenation reactions and are prone to metal aggregation and carbon deposition-induced deactivation. Previous research has shown that the combination of Zr and Cu can produce a synergistic effect, enhancing catalytic performance to a certain extent. The introduction of Zr-Cu bimetals not only improves the acidity and reducibility of the catalyst but also enhances catalytic activity and product selectivity through their synergistic interaction. Therefore, leveraging the synergistic effects between metals and the spatial confinement effect of mesoporous materials on reactants has become a critical research direction. Recent studies have emphasized the importance of bimetallic synergies and pore structure engineering for biomass pyrolysis (Yu *et al*.) reported that mesoporous structure regulation can enhance mass transfer, while Li *et al*. found that Cu-based bimetallic catalysts improve hydrogenation selectivity. However, few studies have combined Zr-Cu bimetals with MCM-41 to simultaneously optimize deoxygenation, hydrogenation, and mass transfer, which is the core of this work.[10,16]

In this study, the focus is on the development of a Zr-Cu bimetallic catalyst supported on mesoporous MCM-41 (with an average pore diameter of 3.8 nm) for the co-pyrolysis of oleic acid and methanol, with the objective of efficiently producing hydrocarbon-rich biofuels. The core design is based on the synergistic interaction between the bimetallic active sites and the mesoporous carrier. Zr provides acidic sites to promote the deoxygenation of oxygenated intermediates, while Cu offers hydrogenation active sites to saturate unsaturated hydrocarbons. This dual-function synergy enables the precise regulation of product distribution. Meanwhile, the ordered mesoporous structure of MCM-41 enhances reactant adsorption, product diffusion, and the local stability of reaction intermediates, thereby further enhancing catalytic activity and long-term stability. Experimental results indicate that the optimized 2Zr-Cu/MCM-41 catalyst exhibits outstanding performance. Under reaction conditions of 500 °C, an alcohol-to-oil ratio of 5:1, and a catalyst dosage of 1 g, it achieves 100% conversion of oleic acid, 90.6% hydrocarbon selectivity, and a 76.7% yield of C_8-C_{17} fractions (meeting the specifications of aviation-grade biofuels). Additionally, it demonstrates stable catalytic activity over three cycles and excellent coke resistance. Compared to recent studies on monometallic or other bimetallic systems (*e.g*., Ni-Cu, Co-Mo), the present work uniquely integrates Zr and Cu on a mesoporous MCM-41 support to achieve synergistic deoxygenation and hydrogenation, enabling high selectivity toward C_8-C_{17} hydrocarbons under mild conditions.

2. Experimental

2.1 Experimental raw materials and instruments

Oleic acid was purchased from Guangdong Guanghua Science and Technology Co., Ltd., methanol (CH_3OH), zirconium nitrate pentahydrate ($Zr(NO_3)_4{\cdot}5H_2O$), and copper nitrate hexahydrate ($Cu(NO_3)_2{\cdot}6H_2O$) were sourced from Shanghai Aladdin Biochemical Science and Technology Co., Ltd., The mesoporous materials MCM-41 (SiO_2/Al_2O_3=28), Lay (SiO_2/Al_2O_3=5.5), ZSM-5 (SiO_2/Al_2O_3=25), and Hβ (SiO_2/Al_2O_3=2.5) were obtained from Tianjin Nanhua Catalyst Co., Ltd.

The following instruments were used in the experiments: D8 Advance X-ray diffractometer (Bruker AG, Germany), JEM-2100F transmission electron microscope (JEOL AG, Japan), Regulus 8100 scanning electron microscope (Hitachi AG, Japan), TENSOR 27 Fourier-transform infrared spectrometer (Bruker AG, Germany), TG 209F3 thermogravimetric analyzer (NETZSCH Instrument Manufacturing GmbH, Germany), ASAP2020 fast specific surface area and pore size analyzer (Micromeritics Instrument Corporation, USA), TP-5080 automatic multi-purpose adsorption analyzer (Tianjin Xianquan Industry and Trade Development Co., Ltd., Tianjin, PR China), AZ-FX-100 pyrolysis reactor system (Tianjin Aozhan Technology Co., Ltd., Tianjin, PR China), and ITQ900 gas chromatography-mass spectrometry (GC-MS) system (Thermo Fisher Scientific, USA).

2.2 Catalyst preparation

The MCM-41, HZSM-5, LaY, and Hβ molecular sieves were

[3]*Engineering Research Center of Metallurgical Energy Conservation and Emission Reduction, Ministry of Education, Kunming University of Science and Technology, Kunming, 650093, China*
[*]*Email:* xianghong-li@163.com (Xianghong Li), xujuan@swfu.edu.cn (Juan Xu)

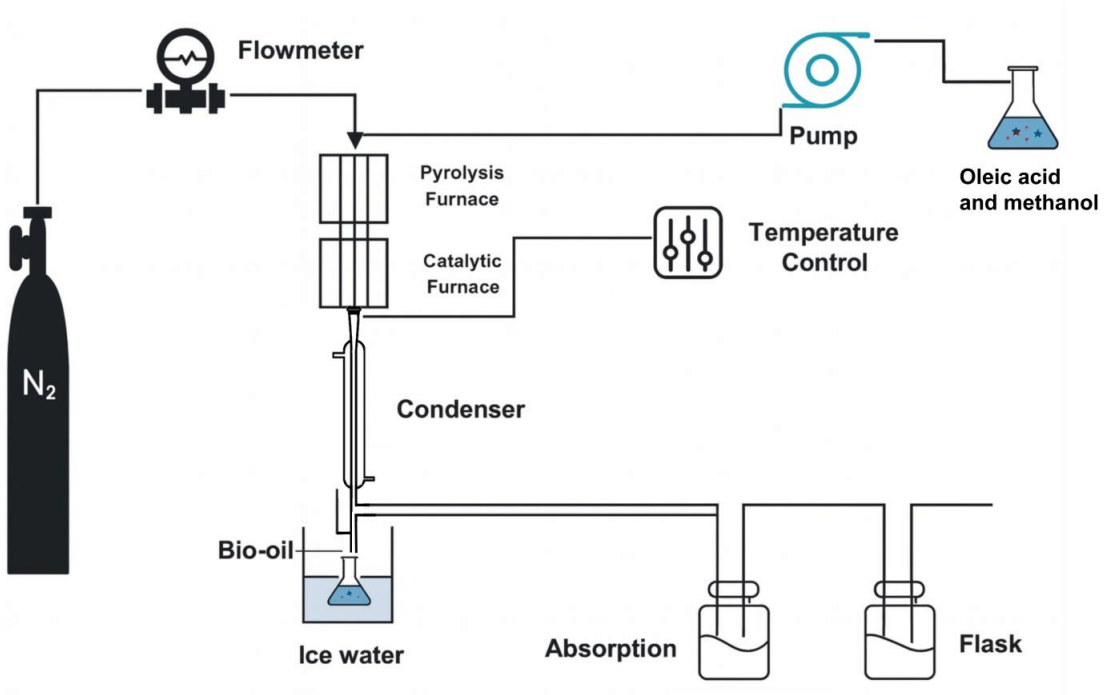

Fig. 1: Schematic diagram of the fixed-bed reactor system.

initially dried under vacuum at 150 °C for 12 h, followed by calcination in a muffle furnace at 550 °C for 5 h to achieve activation.

Single-metal catalysts (12% Zr/MCM-41, 12% Cu/MCM-41) and bimetallic catalysts (xZr-yCu/MCM-41) with varying component gradients were synthesized via the incipient wetness impregnation method. Zirconium nitrate ($Zr(NO_3)_4{\cdot}5H_2O$) was dissolved in deionized water, and copper nitrate ($Cu(NO_3)_2{\cdot}6H_2O$) was dispersed in absolute ethanol. Subsequently, 3.0 g of the pretreated MCM-41 support was immersed into the mixed solution and continuously stirred at 80 °C in an oil bath. After slow evaporation of the solvent, the resultant solid was dried under vacuum at 120 °C for 5 h. The solid was then calcined in a temperature-programmed furnace (heating rate: 5 °C/min up to 550 °C, held for 4 h). Finally, the catalyst was reduced in a tubular furnace at 550 °C for 4 h with a heating rate of 5 °C/min in a H_2/Ar mixture (H_2 volume fraction: 10%) to obtain the target catalyst.

2.3 Catalytic reaction

The catalytic performance was evaluated using a fixed-bed microreactor (Fig. 1). A specific amount of catalyst was uniformly dispersed in a stainless-steel reaction tube, supported by a quartz cotton bed. Before starting the system, the reactor was purged with high-purity nitrogen (99.999%) to evacuate oxygen and ensure that the reaction occurred in an oxygen-free environment. After establishing the inert atmosphere, the reactor was heated to the desired temperature (400-550°C). A mixed solution of oleic acid and methanol was then fed into the vaporization chamber at a constant flow rate using a high-pressure constant flow pump. Once the temperature stabilized, the reaction was allowed to proceed for 30 minutes. The pyrolysis products were then cooled and collected using a condensing device.

The products were analyzed using an ITQ900 gas chromatography-mass spectrometry (GC-MS) system equipped with an HP-5MS capillary column (30 m × 0.25 mm × 0.25 μm). Qualitative identification was achieved by comparing the obtained mass spectra with a standard reference library. Quantitative analysis was performed based on the total ion chromatogram (TIC) using the peak area normalization method. The conversion of oleic acid and the selectivity of products were calculated according to Eq. (1) and (2).

$$\eta=\left(\frac{m_0-m_1}{m_0}\right)\times 100\% \quad (1)$$

$$S=\frac{W_i}{W_p}\times 100\% \quad (2)$$

η-conversion rate of oleic acid, %; m_0-mass of oleic acid of raw material, g; m_1-mass of oleic acid after reaction, g; S-selectivity of hydrodeoxygenation reaction product, %; W_i-mass fraction of a certain product in the product, %; W_p-total mass fraction of product, %.

GC-MS Analysis Conditions: High-purity helium was used as the carrier gas with a split ratio of 10:1. The injector temperature was set at 280 °C. The column oven was temperature-programmed as follows: held at 50 °C for 5 min, then raised to 280 °C at a rate of 5 °C • min^{-1}, and finally held at 280 °C for an additional 5 min. For mass spectrometric detection, electron ionization (EI) was employed at an ionization energy of 70 eV. The ion source temperature was

maintained at 230 °C, with a mass scan range of m/z 30-500.

3. Results and discussion

3.1 Molecular sieve selection

The XRD patterns of the molecular sieves are displayed in Fig. 2(a). As illustrated in the figure, the presence of sharp diffraction peaks for ZSM-5, Hβ, and Lay indicates the existence of crystalline structures within these molecular sieves. In contrast, the MCM-41 molecular sieve exists in an amorphous structural form.[17] The XRD pattern of Lay displays hallmark Y zeolite characteristics, exhibiting sharp and symmetrical reflections at the[111],[220],[331],[533],[555] planes, indicative of the FAU structure.[18] The ZSM-5 sample displays characteristic peaks that are indicative of the MFI zeolite type at 8° and 23°.[19] Hβ molecular sieve exhibits diffraction peaks at 7.80°, 13.44°, 21.41°, 22.43°, 25.30°, 27.03°, 28.72°, and 29.53°, all of which are characteristic diffraction peaks attributable to the BEA topology of Hβ molecular sieve.[20]

The structural characteristics of molecular sieves are shown in Table 1. As shown in the table, MCM-41 has the largest specific surface area (728 m^2/g), followed by Lay (687 m^2/g). ZSM-5 has the smallest specific surface area, at 341 m^2/g. MCM-41 has an average pore diameter of 3.8 nm and is predominantly mesoporous. Studies indicate that the specific surface area and pore size of catalysts significantly influence their performance, with larger surface areas facilitating pyrolysis reactions.

The conversion rate of oleic acid and product distribution for common molecular sieves are shown in Fig. 2(b), Fig. 2(c) and Table 2. As demonstrated in Table 2, in the absence of a molecular sieve catalyst, the oleic acid conversion rate was a mere 10.21%, and the hydrocarbon content is just 4.23%. In the context of molecular sieve utilization as catalysts, oleic acid conversion rates exhibit the following sequence: Lay > MCM-41 > Hβ > ZSM-5. In addition, both Lay and MCM-41 achieved hydrocarbon yields that exceeded 20%, thereby outperforming Hβ and ZSM-5. As illustrated in Fig. 2(b) and Fig. 2(c), the distribution of oleic acid pyrolysis products exhibits substantial variation among diverse molecular sieve catalysts. The C_8-C_{17} hydrocarbon yield achieved by Lay was 16%, followed by MCM-41 with a yield of 10%. The other two molecular sieves yielded even lower C_8-C_{17} hydrocarbon yields. This finding suggests that molecular sieves are not directly applicable for oleic acid pyrolysis catalysis. Although Lay exhibited the highest initial oleic acid conversion and C_8-C_{17} hydrocarbon yield among the tested molecular sieves, MCM-41 was selected as the support for bimetallic catalyst preparation due to its well-defined mesoporous structure, larger pore size (3.8 nm), and higher specific surface area (728 m^2/g), which are more conducive to metal dispersion, reactant diffusion, and active site accessibility during catalytic pyrolysis. In order to further enhance hydrocarbon yields, bimetallic catalysts were prepared using MCM-41 molecular sieve, which are known for their superior catalytic performance, as supports. This improvement in catalytic activity was achieved through the use of MCM-41 molecular sieve.

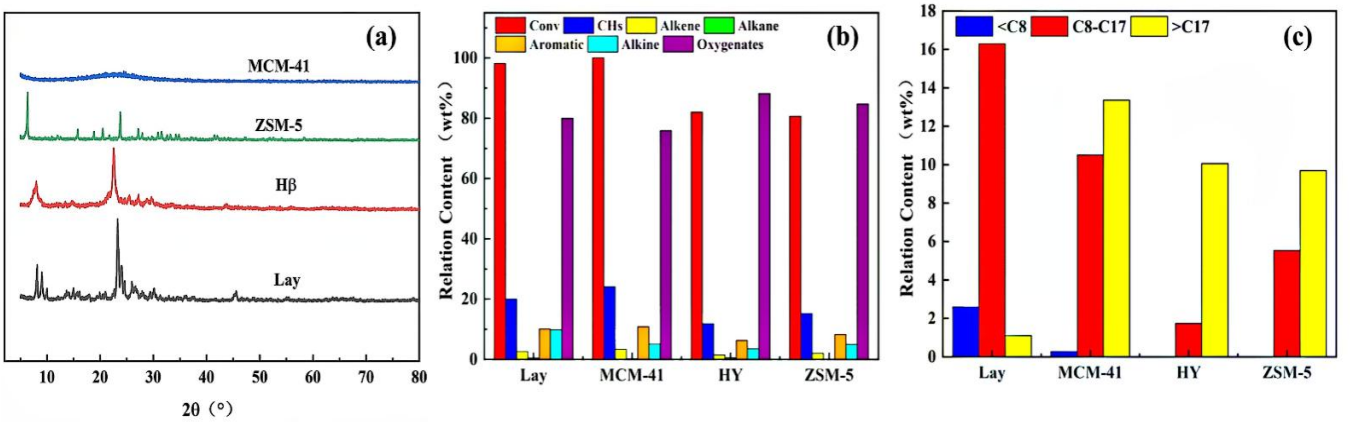

Fig. 2: (a) XRD profiles of the four molecular sieves (MCM-41, Lay, ZSM-5, Hβ); (b) oleic acid conversion and (c) hydrocarbon product distribution from their catalytic pyrolysis.

Table 1: Specific surface area, mean pore diameter and total pore volume of four molecular sieves.

Molecular Sieve	BET(m^2/g)	Mean pore diameter(nm)	Total pore volume(cm^3/g)
MCM-41	728	3.8	0.39
Lay	687	2.3	0.24
ZSM-5	341	0.5	0.15
Hβ	602	2.9	0.43

Table 2: Pyrolysis products and conversion rate of oleic acid produced by common molecular sieves.

Molecular Sieve	Conversion（%）	Hydrocarbon Content(%)
ZSM-5	80.65	15.23
Hβ	82.47	11.81
MCM-41	98.22	20.24
Lay	100	24.12
None	10.21	4.23

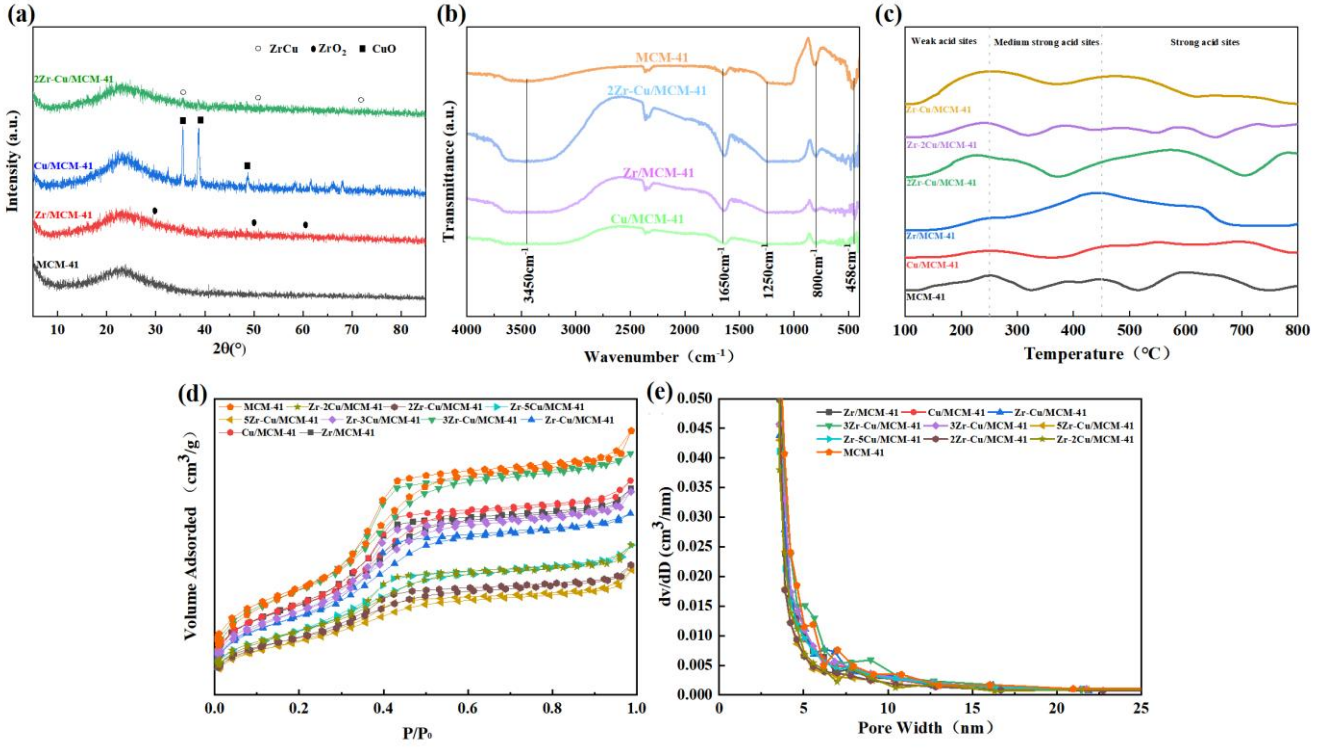

Fig. 3: (a) XRD pattern of catalysts, (b) FT-IR spectra , (c) NH_3-TPD profiles, (d) N_2 adsorption-desorption isotherm, (e) pore size distribution.

3.2 Catalyst characterization

The XRD spectrum of the catalyst is shown in Fig. 3(a). It can be seen from the figure that the framework of molecular sieves has not changed after metal loading. In the single metal catalyst system, ZrO_2 characteristic peaks appear in Zr/MCM-41, 2θ=35.7°, 51.5°, 64.3°, corresponding to (110), (200), (211) crystal planes respectively, and PDF standard card of monoclinic zirconia (m-ZrO_2) (PDF #00-034-0657) shows high agreement.[21] CuO characteristic peaks appear in Cu/MCM-41, 2θ=35.5°, 38.7°, 48.8°, corresponding to (111), (111), (202) crystal planes respectively, which is consistent with the PDF standard card of monoclinic copper oxide (m-CuO) (PDF #00-048-1548),[22] indicating that Zr and Cu species exist in oxidized states when loaded on MCM-41 alone. Diffraction patterns of bimetallic catalyst 2Zr-Cu/MCM-41 show significant differences, with no obvious ZrO_2 and CuO crystal characteristic peaks, and the broadened dispersion peaks indicate that metal components are highly dispersed in the mesoporous framework. The new diffraction peaks at 2θ=35.6°, 50.9° and 70.6° are different from those of ZrCu alloy standard card (PDF #00-022-0233), corresponding to (110), (201) and (112) crystal planes respectively, indicating that Zr and Cu formed a Zr-Cu alloy phase during loading.

The FT-IR spectra of the MCM-41 support and its supported Cu, Zr monometallic, and 2Zr-Cu bimetallic catalysts are shown in Fig. 3(b). The characteristic peaks at 3450 cm^{-1} and 1650 cm^{-1} correspond to the hydroxyl stretching vibration and bending vibration of adsorbed water on the catalyst and support surfaces, respectively. The Si-O-Si vibrational peaks at 1250 cm^{-1} and 800 cm^{-1}, along with the Si-O bending vibration peak at 458 cm^{-1}, reflect the structural features of the Si-O framework of the MCM-41 support.[23] After metal loading, the intensity of the 1650 cm^{-1} peak increased in Cu/MCM-41, Zr/MCM-41, and 2Zr-Cu/MCM-41 compared to MCM-41, indicating the formation of hydrogen bonds and coordination bonds between the metal and the hydroxyl groups on the support surface.[24] This led to an increase in adsorption sites, enhancing the adsorption capacity for water molecules and increasing the surface water content.[25]The peak intensities at 1250 cm^{-1} and 800 cm^{-1}

decreased after metal loading, which may be due to the disruption of the original ordered Si-O framework structure. The metal atoms likely embedded or attached to the Si-O skeleton, disturbing the periodic arrangement of Si-O-Si bonds, leading to disordered bond vibrations and a reduction in dipole moment change, which resulted in the decreased peak intensity.[26,27] The Si-O bending vibration peak at 458 cm^{-1} weakened after metal loading, possibly due to the suppression of Si-O bending vibrations by the metal atoms. The interaction between the metal atoms and Si-O bonds may have increased the rigidity of the Si-O bonds, restricting bending vibrations, reducing dipole moment changes, and consequently diminishing the absorption peak intensity.[28] The peak shape at 2384 cm^{-1} for 2Zr-Cu/MCM-41 differs from that of Zr/MCM-41 and Cu/MCM-41, suggesting that new vibrational modes or adsorbed species may have formed under the synergistic effect of the bimetallic materials.[29]

The adsorption-desorption curves, pore size distribution, and structural characteristics of MCM-41 and its supported catalysts with different metals (both single-metal and bimetallic) are presented in Fig. 3(d, e) and Table 3. As shown in Fig. 3(d), the adsorption-desorption isotherms are of type IV. In the low relative pressure region, the adsorption capacity increases rapidly, corresponding to the adsorption of monolayer to multilayer molecules. In the high relative pressure region, hysteresis loops appear, indicating the capillary condensation phenomenon in the mesoporous structure. This confirms that the sample exhibits the pore structure characteristics typical of mesoporous materials.[30] The adsorption capacity of N_2 molecules decreases after metal loading, likely due to the metal occupying part of the pores or altering the internal surface properties, which hinders N_2 adsorption.[31] As shown in Fig. 3(e), the pore size of each sample is concentrated between 2-5 nm, consistent with the mesoporous characteristics of MCM-41. The average pore size of MCM-41 is 3.5 nm. After metal loading, the average pore size of Zr-Cu/MCM-41 increases to 4.0 nm. This change suggests that metal loading affects the pore structure, with some pores being modified or blocked by the metal, resulting in a relative increase in larger pores. Although the average pore size increases, the extent of this change varies, reflecting the impact of different metal loadings and loading methods on the pore structure.

Based on the data analysis presented in Table 3, the specific surface area of MCM-41 is 728 m^2/g. After metal loading, the specific surface area generally decreases, likely due to the aggregation of metal particles within the pores. Additionally, the interaction between the metal and silanol groups during high-temperature calcination may cause the collapse of the pore walls. Together, these factors lead to a reduction in the effective surface area available for N_2 adsorption.[32] The average pore volume of MCM-41 is 0.39 cm^3/g. For most of the metal-loaded samples, the pore volume decreases, which can be attributed to the spatial restriction caused by the metal nanoparticles within the pores. This results in a significant reduction in the effective adsorption space, as the entrances to micropores and mesopores become blocked. However, the average pore volume of 3Zr-Cu/MCM-41 is 0.37 cm^3/g, which is similar to that of MCM-41. This suggests that, under this particular metal loading ratio, the metal is more evenly distributed within the pores, having little impact on the pore volume. These findings indicate that different metal loading ratios lead to varying changes in the catalyst's pore structure, which may subsequently affect its catalytic performance. The surface area of bimetallic-supported catalysts is smaller than that of single-metal-supported catalysts, likely due to the formation of a Zr-Cu alloy. This alloy may block pores and cause metal particles to occupy the pores, altering the pore wall structure and resulting in a decrease in the specific surface area.[33,34] Although metal loading led to a reduction in specific surface area, the introduced Zr-Cu alloy phase provided abundant active sites for deoxygenation and hydrogenation. This trade-off between surface area loss and active site generation ultimately contributed to the enhanced catalytic performance of 2Zr-Cu/MCM-41.

The NH_3-TPD curves for MCM-41, Zr/MCM-41, Cu/MCM-41, and 2Zr-Cu/MCM-41 catalysts are shown in Fig. 3(c). Based on the desorption peak temperatures, the solid surface acidity can be categorized into strong acid sites (>450°C), medium-strength acid sites (250-450°C), and weak acid sites (150-250°C).[35] According to previous studies, the amount of acid sites in a catalyst can be reflected

Table 3: Structural characteristics of catalysts.

Catalyst	BET(m^2/g)	Mean pore diameter(nm)	Total pore volume(cm^3/g)
MCM-41	728	3.5	0.39
Zr-Cu/MCM-41	372	4.0	0.27
2Zr-Cu/MCM-41	613	3.8	0.15
3Zr-Cu/MCM-41	396	3.9	0.37
5Zr-Cu/MCM-41	384	4.1	0.14
Zr/MCM-41	719	3.9	0.26
Zr-2Cu/MCM-41	441	3.9	0.19
Zr-3Cu/MCM-41	541	3.9	0.29
Zr-5Cu/MCM-41	576	3.9	0.19
Cu/MCM-41	615	3.8	0.30

by the peak area.[36]

For MCM-41, a distinct desorption peak is observed in the low-temperature region (approximately 150-250°C), indicating the presence of weak acid sites. However, in the temperature ranges corresponding to medium and strong acid sites, the desorption peaks are not prominent, suggesting that MCM-41 has relatively low overall acidity. After Cu loading, the peak area in the weak acid region of Cu/MCM-41 changed, and new features appeared in the medium-strength acid region (250-450°C). This may be attributed to the influence of Cu addition, which altered the distribution of acid sites and formed some medium-strength acid sites,[37] although strong acid sites were still not significant. In contrast, the acidity of the Zr/MCM-41 catalyst showed significant changes. The strong acid sites became the dominant acidic contributors, with a slight desorption peak in the high-temperature region (>450°C) corresponding to the strong acid sites, although the total number of strong acid sites remained relatively limited.[38] The 2Zr-Cu/MCM-41 catalyst exhibited clear desorption peaks across different temperature ranges. The weak acid site peaks were still present, the peak area in the medium-strength acid region increased, and the desorption peak for strong acid sites became more prominent. This indicates that the synergistic effect of Zr and Cu generates more strong acid sites, significantly enhancing both the acid strength and acid content, and broadening the distribution of acid sites. The desorption peaks of Zr-2Cu/MCM-41 differ from those of 2Zr-Cu/MCM-41, especially in the shape and area of peaks in the medium- and strong-acid regions. This reflects the important influence of the Zr/Cu ratio on the acidity characteristics, demonstrating that the content and ratio of Zr and Cu are key factors in regulating the formation and distribution of acid sites.[39] Zr-Cu/MCM-41 shows a unique desorption peak distribution. Compared to other catalysts, the peak areas and positions in different acid strength regions exhibit distinct acidic characteristics, indicating that the structure and chemical environment of Zr and Cu complexes on MCM-41 alter the properties of the acid sites. The increased acid center density and strength enhance the deoxygenation efficiency and overall catalytic performance of the catalyst.[40]

The SEM images of the molecular sieves and catalysts are shown in Fig. 4(a). The mesoporous MCM-41 (Fig. 4 (a_1)) exhibits an ordered honeycomb-like porous structure with relatively uniform dispersion and minimal agglomeration. However, the surface morphology of Zr/MCM-41 (Fig. 4(a_2)) and Cu/MCM-41 (Fig. 4(a_3)) shows some changes, likely due to the introduction of metal, which may alter the material's growth mechanism or partially fill the pore structure. As the Zr/Cu ratio changes, the surface roughness and pore structure of 2Zr-Cu/MCM-41 (Fig. 4(a_4)), Zr-2Cu/MCM-41 (Fig. 4(a_5)), and Zr-Cu/MCM-41 (Fig. 4(a_6)) become increasingly complex. These morphological changes may influence the specific surface area, pore size distribution, and the exposure of active sites, thereby affecting the catalytic activity and selectivity.[41]

The EDS analysis of the 2Zr-Cu/MCM-41 catalyst is shown in Fig. 4(b). The element distribution map reveals that O, Al, and Si are uniformly distributed across the entire sample, which is likely related to the oxygen and silicon-aluminum framework structure of the MCM-41 support. The distribution of Cu and Zr, on the other hand, shows some aggregation, suggesting that these metals may exist in the form of particles or clusters within the catalyst. This distribution could be influenced by the loading method of Cu and Zr and their interaction with the MCM-41 support.[42] The EDS spectra show characteristic peaks for the different elements, with O, Al, and Si displaying higher peak intensities, indicating that these elements occupy a larger proportion of the sample. Although the peaks for Cu and Zr are relatively low, they are still clearly visible, confirming the successful loading of these metals onto MCM-41.[43] According to the elemental content data, O has the highest content (54.83%), followed by Si (26.33%) and Al (1.06%), which aligns with the chemical composition of MCM-41. The contents of Cu and Zr are 6.67% and 11.11%, respectively, which is close to the calculated values, confirming the successful metal loading.

Fig. 4(c) shows the TEM images of MCM-41 and

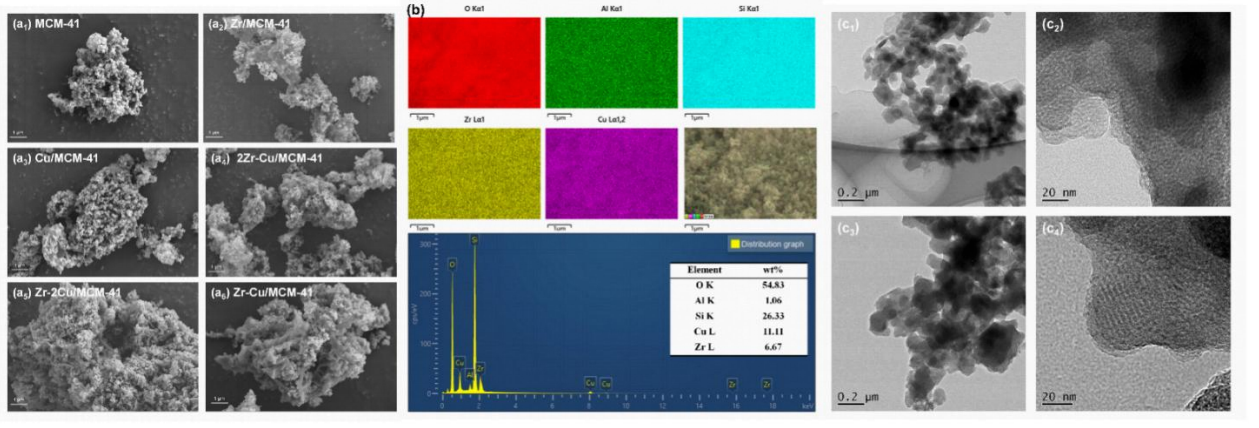

Fig. 4: (a) SEM images of MCM-41 molecular sieve and catalysts, (b) EDS spectrum of the 2Zr-Cu/MCM-41 catalyst, (c) TEM images of MCM-41 molecular sieve(c_1, c_2) and the 2Zr-Cu/MCM-41 catalyst (c_3, c_4).

2Zr-Cu/MCM-41 catalysts, further confirming the honeycomb mesoporous structure of both MCM-41 and the prepared catalysts. The TEM image of MCM-41 in Fig. 4(c_1) reveals a relatively clear porous structure, with a regular and uniform pore distribution. This ordered pore structure provides an efficient mass transfer channel for reactants, increasing the contact area between the catalyst and the reactants, reflecting the inherent characteristics of the MCM-41 support. Fig. 4(c_2) further highlights the finer pore features. The layered or fibrous structure of the pore walls suggests that MCM-41 has a significant specific surface area and porosity, which is beneficial for adsorption and catalytic reactions.[44] The TEM image of 2Zr-Cu/MCM-41 in Fig. 4(c_3) shows some particulate matter dispersed within the pores or on the surface, likely corresponding to the loaded Zr and Cu components. Fig. 4(c_4) provides a clearer view of these metal particles, which are small and well-dispersed in the MCM-41 pores. This indicates that Zr and Cu have been successfully loaded onto MCM-41 without excessive aggregation.[41] The combination of these metal particles with the MCM-41 support enhances the catalyst's active sites, while the porous structure remains intact, providing favorable conditions for catalytic reactions

3.3 Catalytic performance characterization

The effects of Zr/MCM-41, Cu/MCM-41, and bimetallic catalysts with varying Zr-Cu ratios on the conversion and selectivity of oleic acid catalytic pyrolysis to hydrocarbon products were compared. The results are presented in Fig. 5.

Fig. 5 shows that without a catalyst, the conversion of oleic acid is only 10.21%, and the content for hydrocarbon compounds is just 4.23%. The addition of MCM-41 significantly enhances oleic acid conversion, indicating that MCM-41 itself has a promotional effect on the reaction. The Cu/MCM-41 catalyst exhibited poor oleic acid conversion and low hydrocarbon selectivity, while the Zr/MCM-41 catalyst demonstrated higher conversion and greater hydrocarbon yield. This is likely attributed to the acidity and specific surface area of the catalyst.[45,46] The BET test results show that Zr/MCM-41 has a specific surface area of 719 m^2/g, which is larger than the 615 m^2/g surface area of Cu/MCM-41. This difference in surface area may account for the higher catalytic activity observed in Zr/MCM-41 compared to Cu/MCM-41.[46] Compared to the molecular sieve alone, the bimetallic catalyst significantly improves the conversion of oleic acid. As the Zr/Cu ratio increases from 1:2 to 2:1, the conversion increases from 58.6% to 100%, the deoxidation efficiency improves, and the hydrocarbon yield reaches 90.6%. Concurrently, with increasing Zr content, the content of aromatic hydrocarbons and C_8-C_{17} hydrocarbons increases, while the olefin content decreases. This suggests that appropriate metal loading can effectively regulate the carbon chain length of the product and promote the formation of the target product.[47] The high activity of Zr accelerates the pyrolysis reaction; however, excessive Zr content diminishes the catalytic effect. This is because the interaction between Cu and Zr adjusts the ratio of Cu and Cu^+ on the catalyst surface, and too much Zr negatively affects the dispersion of Cu^{2+} on the catalyst surface.[48] With 2Zr-Cu/MCM-41 as the catalyst, oleic acid is almost completely converted, yielding 90.6% hydrocarbon compounds, and 76.7% of these hydrocarbons fall within the C_8-C_{17} range suitable for aviation fuel. This is likely due to the greater number of acidic sites on the Zr-modified catalyst.[49] The 2Zr-Cu/MCM-41 catalyst has the highest acid value and acidity, particularly in the strong acid sites. Additionally, it has the best physical properties, including specific surface area and particle size, which contribute to its outstanding catalytic performance.

Based on the analysis of pyrolysis products, this study proposes a plausible reaction mechanism (Fig. 6). Oleic acid initially undergoes primary pyrolysis, generating a series of

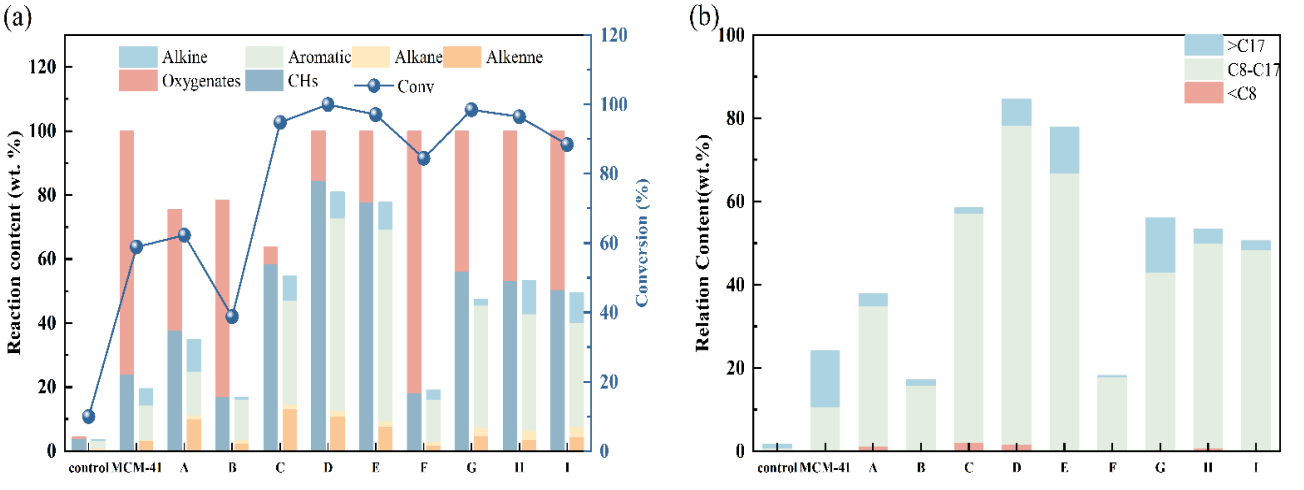

Fig. 5: Effect of different catalyst compositions on oleic acid conversion and product distribution.
(A: Zr/MCM-41; B: Cu/MCM-41; C: Zr-Cu/MCM-41; D: 2Zr-Cu/MCM-41; E: 3Zr-Cu/MCM-41; F: 5Zr-Cu/MCM-41; G: Zr-2Cu/MCM-41; H: Zr-3Cu/MCM-41; I: Zr-5Cu/MCM-41).

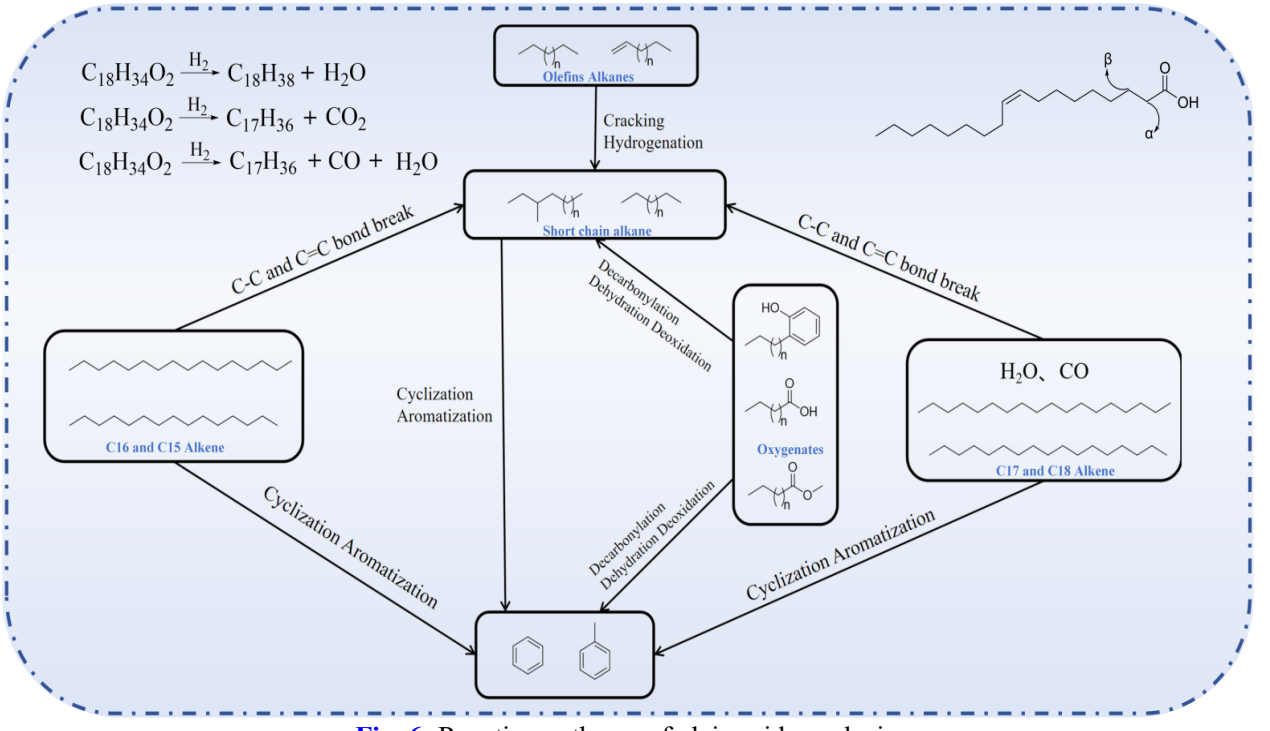

Fig. 6: Reaction pathway of oleic acid pyrolysis.

products including short-chain alkenes, alkanes, and oxygenated compounds. The detected heptene in the products may originate from decarboxylation and decarbonylation pathways of oleic acid, while the presence of C_{17} and C_{18} saturated alkanes further supports the occurrence of decarboxylation reactions. Furthermore, the abundant saturated hydrocarbons with C-C single bonds in the products are suggested to form via subsequent hydrogenation and stabilization of unsaturated radicals generated by β-scission of C-C bonds. The oxygenated compounds derived from pyrolysis can be further converted into hydrocarbons through reactions such as decarboxylation and decarbonylation under catalytic action, with oxygen removed in the form of CO, CO_2, and H_2O. The introduced methanol can be dehydrated over the catalyst to form dimethyl ether, both of which serve as important hydrocarbon pool precursors. They participate in a series of carbon-chain building reactions, such as alkylation and oligomerization, to form alkenes. Meanwhile, methanol may also act as a hydrogen donor, facilitating the hydrodeoxygenation of intermediates such as phenols to form aromatic hydrocarbons. The catalyst Zr-Cu/MCM-41 plays multiple critical roles in the reaction system: on one hand, it catalyzes the aromatization of alkenes to form aromatics; on the other hand, methanol provides a methyl source, promoting the methylation of the generated aromatic hydrocarbons. In addition, under high temperature and synergistic catalytic effects, esterification between oleic acid and methanol also occurs, yielding methyl oleate.

As shown in Fig. 7, the conversion rate of oleic acid increases as the pyrolysis temperature rises from 400°C to 550°C. At 500°C, the feedstock is completely converted; however, when the temperature increases further to 550°C, the hydrocarbon content decreases from 90.6% to 70.5%, while the oxygenate content rises from 9.4% to 29.5% (Fig. 7(a)). Additionally, with increasing temperature, the hydrocarbon content in the aviation fuel range increases. At 500°C, the aviation fuel component reaches 76.7% (Fig. 7(b)). This can be attributed to the cracking of oleic acid macromolecules, where the oxidation process absorbs a significant amount of heat. On one hand, higher temperatures lead to secondary cracking of products, generating volatile gases such as CO and CO_2, which promote the breakdown of long-chain hydrocarbons.[50] As a result, the selectivity and content of light alkanes (C_8-C_{17}) improve. On the other hand, elevated temperatures also accelerate the conversion and decomposition of oleic acid. Simultaneously, the endothermic dehydrogenation reactions of methanol and oleic acid further limit the reaction at higher temperatures, as methanol decomposes more rapidly into smaller molecules, reducing the available hydrogen source for the system. This ultimately leads to a decrease in hydrocarbon content and a reduction in the aviation fuel range.[51]

Moreover, as catalytic temperature increases, the conversion of feedstock rises from 27.3% to 100%. The hydrocarbon content initially increases but then decreases significantly. The content of aromatics increases notably with temperature, while olefins and alkanes show a similar trend of first increasing and then decreasing. The oxygenate content decreases as the temperature rises. In parallel, fuels in the gasoline range increase initially but then decrease, while fuels in the C_8-C_{17} range show the opposite trend. Fig. 7(c, d) These changes are due to the combined effects of pyrolysis vapors from the feedstock and reactions on the catalyst surface, such as isomerization, which is a typical endothermic reaction. As

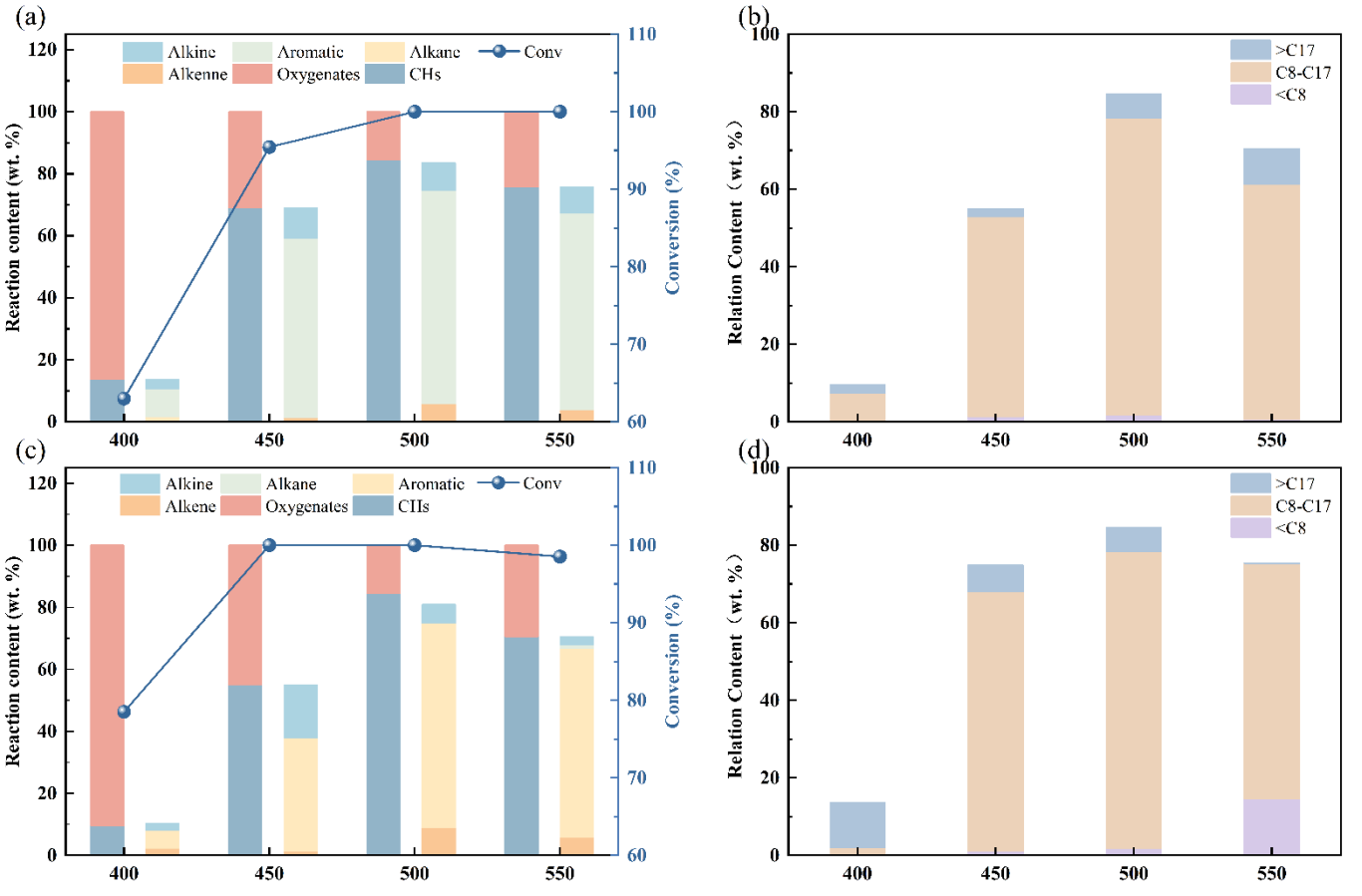

Fig. 7: Effect of pyrolysis temperature (a, b) and catalytic temperature (c, d) on oleic acid conversion and product distribution.

temperature increases, the cracking of oleic acid and the endothermic fracture of long-chain hydrocarbons accelerate, leading to an increase in their content.[52]

Fig. 8 (a, b) illustrate the effect of the alcohol-oil ratio on oleic acid conversion and product selectivity under the conditions of the 2Zr-Cu/MCM-41 catalyst. The data show that the alcohol-oil ratio directly influences the conversion rate of oleic acid. In the absence of the hydrogen source, methanol, the conversion rate of oleic acid is only 48%, with hydrocarbons making up just 35% of the products. As the methanol-to-oleic acid ratio increases, the conversion rate of oleic acid rises, reaching 100% when the alcohol-oil ratio is 3:1. Beyond this point, increasing the alcohol-oil ratio no longer affects the conversion rate, but the hydrocarbon content in the product increases from 35% to 90.6%. This is because methanol provides sufficient hydrogen, enabling oleic acid to undergo deoxygenation through the formation of CO_2 and H_2O. As the alcohol-oil ratio increases, the number of carbon atoms in the hydrocarbon products also increases. This effect may be due to the rising oxygen content in the reaction system, which influences the catalyst's ability to convert oleic acid, thereby affecting the cracking of larger molecules.[53]

Fig. 8 (c, d) demonstrate the impact of catalyst dosage on oleic acid conversion and product selectivity with the 2Zr-Cu/MCM-41 catalyst. The data show that as the catalyst dosage increases, the conversion of hydrocarbons, aromatics, alkanes, and olefins initially increases and then decreases. Similarly, the hydrocarbon content in the $\leq C_8$, C_8-C_{17}, and $\geq$C17 carbon atom ranges follows the same trend. At low catalyst levels (0.5 g), the raw materials tend to polymerize, producing more oxygenates and other by-products. At a catalyst dosage of 1 g, the system achieves higher deoxidation and conversion, likely due to the increased number of active sites on the catalyst surface, allowing for better interaction between oleic acid molecules and active sites, which enhances the reaction and deoxidation activity. However, when the catalyst dosage exceeds 1.5 g, the increased mass transfer and heat transfer resistance hinder the catalytic reaction, resulting in a decrease in both the conversion rate and hydrocarbon content.

3.4. Stability and inactivation analysis of catalysts

After the reaction, the used catalyst was soaked and washed with ethanol, then dried under vacuum. It was subsequently calcined in a tube furnace at 550°C for 4 h to remove any residual organic matter. The catalyst was then reused for the next test under the same reaction conditions. The repeatability test results for the 2Zr-Cu/MCM-41 catalyst, with a pyrolysis temperature of 500°C, catalytic temperature of 500°C, alcohol-to-oil ratio (mass ratio) of 5:1, and catalyst dosage of 1 g, are shown in Fig. 9(a). As seen in Fig. 9(a), although the catalyst's performance slightly decreases after three repeated

cycles, it still maintains good catalytic activity.

XRD and TG methods were used to analyze the amount and nature of coke deposition and its impact on catalyst deactivation during the reforming process for different catalysts. Fig. 9(c) presents the thermogravimetric curves of MCM-41 and the 2Zr-Cu/MCM-41 catalyst before and after use. As shown in the figure, the weight loss of both MCM-41 and 2Zr-Cu/MCM-41 after use is more significant than before, likely due to the combustion of carbon deposits accumulated on their surfaces. The mass loss of 2Zr-Cu/MCM-41 after use is smaller than that of MCM-41, indicating that the addition of metal effectively enhances the anti-coking ability of 2Zr-Cu/MCM-41. Additionally, MCM-41 begins to decompose at a lower temperature, whereas the decomposition temperature of 2Zr-Cu/MCM-41 is higher. This indicates that the addition of metal enhances the catalyst's thermal stability, effectively preventing degradation during high-temperature pyrolysis. These findings suggest that the modified catalyst exhibits improved resistance to coking.[54]

The XRD patterns of the used molecular sieve and catalyst are shown in Fig. 9(b). It can be observed that the molecular sieve maintains its structural integrity before and after the reaction, with only a slight decrease in peak intensity. In the case of the Cu/MCM-41 catalyst, CuO is reduced to Cu after the reaction, with characteristic peaks at $2\theta = 43.3°$, 50.4°, and 74.1°.[41] This is due to the reaction between CuO and carbon

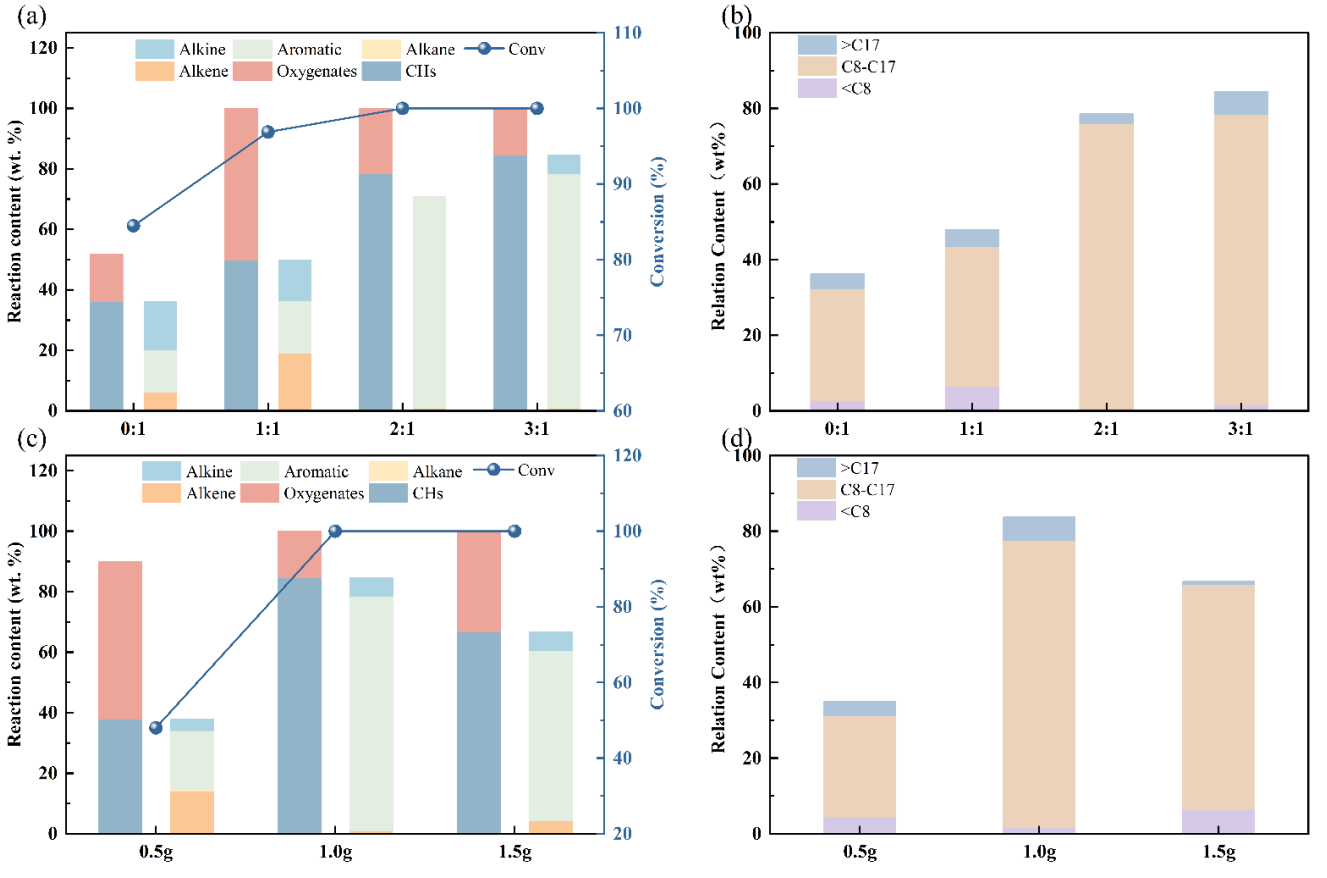

Fig. 8: Effect of alcohol-to-oil ratio (a, b) and catalyst dosage (c, d) on oleic acid conversion and product distribution.

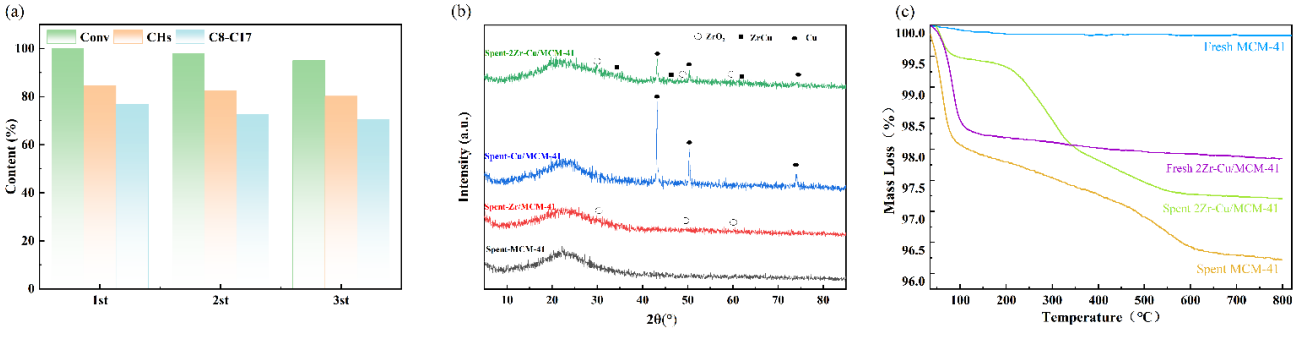

Fig. 9: (a) Recycling performance of the 2Zr-Cu/MCM-41 catalyst, (b) XRD patterns of spent molecular sieve and catalysts, (c) TG profiles of the fresh and spent samples.

at high temperatures during the catalytic process, where oxygen atoms are eliminated as CO_2, causing the disappearance of CuO peaks. In the 2Zr-Cu/MCM-41 catalyst, some of the Cu in the ZrCu alloys is first oxidized to CuO and then reduced to Cu by carbon, which explains the appearance of Cu characteristic peaks in this catalyst. Overall, both the molecular sieve and catalyst retain their original framework structure before and after use, which also explains why the catalyst maintains its catalytic activity after repeated use.

4. Conclusion

This study investigated the catalytic pyrolysis of oleic acid using a ZrCu bimetallic catalyst supported on mesoporous MCM-41. The results demonstrate that the bimetallic catalyst notably improves the conversion of oleic acid and the selectivity of hydrocarbons. Specifically, the 2Zr-Cu/MCM-41 catalyst attains a conversion rate of 100% and a hydrocarbon yield of 90.6%, among which 76.7% falls within the C_8-C_{17} aviation fuel range. The synergistic effect between Zr and Cu, in conjunction with the mesoporous structure of MCM-41, effectively facilitates deoxygenation and hydrogenation reactions, thereby resulting in the generation of target hydrocarbon products. The catalyst demonstrates favorable stability and resistance to coke formation, maintaining its catalytic performance after three reaction cycles. These discoveries emphasize the potential of the ZrCu/MCM-41 catalyst for efficient biomass conversion, providing valuable perspectives for the development of bimetallic catalytic systems in biofuel production.

Acknowledgments

This work was supported by the National Natural Science Foundation of China (32360362), the Joint Key Project of Agricultural Fundamental Research in Yunnan Province (202301BD070001-158).

Conflict of Interest

There is no conflict of interest.

Supporting Information

Not applicable.

CRediT Statement

Chunxia Song: Conceptualization, Methodology, Investigation, Data curation, Writing - Original draft. **Kai Zhang:** Methodology, Validation, Formal analysis. **Naidong Li:** Software, Formal analysis, Visualization. **Xiaoqing Yan:** Resources, Investigation, Data curation. **Fashe Li:** Validation, Resources, Project administration. **Xianghong Li:** Supervision, Writing-Review & editing, Funding acquisition. **Juan Xu:** Supervision, Writing - Review & editing, Project administration.

References

[1] C. H. Geissler, J. Ryu, C. T. Maravelias, The future of biofuels in the United States transportation sector, *Renewable and Sustainable Energy Reviews*, 2024, **192**, 114276, doi: 10.1016/j.rser.2023.114276.

[2] D. Mohan, C. U. Pittman Jr, P. H. Steele, Pyrolysis of wood/biomass for bio-oil: a critical review, *Energy & Fuels*, 2006, **20**, 848-889, doi: 10.1021/ef0502397.

[3] H. M. Salem, D. R. Abdelhafiz, A. M. Matloob, Optimizing green diesel-like hydrocarbons from direct hydrodeoxygenation of oleic acid using Zr-MOF/SBA-3 catalyst, *Journal of Chemical Technology & Biotechnology*, 2025, **100**, 1105-1116, doi: 10.1002/jctb.7847.

[4] M. Jahirul, M. Rasul, A. Chowdhury, N. Ashwath, Biofuels production through biomass pyrolysis: a technological review, *Energies*, 2012, **5**, 4952-5001, doi: 10.3390/en5124952.

[5] F. Alizad Oghyanous, C. Eskicioglu, Hydrothermal liquefaction *vs*. fast/flash pyrolysis for biomass-to-biofuel conversion: new insights and comparative review of liquid biofuel yield, composition, and properties, *Green Chemistry*, 2025, **27**, 7009-7041, doi: 10.1039/d5gc01314c.

[6] P. Talwar, M. A. Agudelo, S. Nanda, Pyrolysis process, reactors, products, and applications: a review, *Energies*, 2025, **18**, 2979, doi: 10.3390/en18112979.

[7] M. Arumugam, C. K. Goh, Z. Zainal, S. Triwahyono, A. F. Lee, K. Wilson, Y. H. Taufiq-Yap, Hierarchical HZSM-5 for catalytic cracking of oleic acid to biofuels, *Nanomaterials*, 2021, **11**, 747, doi: 10.3390/nano11030747.

[8] B. Luna-Murillo, M. Pala, A. L. Paioni, M. Baldus, F. Ronsse, W. Prins, P. C. A. Bruijnincx, B. M. Weckhuysen, Catalytic fast pyrolysis of biomass: catalyst characterization reveals the feed-dependent deactivation of a technical ZSM-5-based catalyst, *ACS Sustainable Chemistry & Engineering*, 2021, **9**, 291-304, doi: 10.1021/acssuschemeng.0c07153.

[9] M. do Carmo Rangel, F. M. Mayer, M. da Silva Carvalho, G. Saboia, A. M. de Andrade, Selecting catalysts for pyrolysis of lignocellulosic biomass, *Biomass*, 2023, **3**, 31-63, doi: 10.3390/biomass3010003.

[10] S. Yu, L.-H. Chen, M.-Y. He, B.-L. Su, Pore science and engineering: a new era of porous materials, *National Science Review*, 2025, **12**, doi: 10.1093/nsr/nwaf258.

[11] C. Mondelli, M. A. González, F. Albergamo, C. Carbajo, M. J. Torralvo, E. Enciso, F. J. Bermejo, R. Fernández-Perea, C. Cabrillo, V. Leon, M. L. Saboungi, Collective excitations in liquid D_2 confined within the mesoscopic pores of a MCM-41 molecular sieve, *Physical Review B*, 2006, **73**, 094206, doi: 10.1103/physrevb.73.094206.

[12] S.L. Ma Dong, Wang Zhibin, Chen Lei, Yang Shuangxia, Xu Meirong, Xie Xinping, Si Hongyu, Zhao Baofeng, Gao Mingjie, Li Tianjin, Hua Dongliang, Research Progress on the Direct Synthesis of Aromatics From Syngas by Oxygen-

Containing Intermediates, *Acta Petrolei Sinica(Petroleum Processing Section)*, 2024, **40**, 248-257, doi: 10.3969/j.issn.1001-8719.2024.01.025.

[13] S. Kattel, B. Yan, Y. Yang, J. G. Chen, P. Liu, Optimizing binding energies of key intermediates for CO_2 hydrogenation to methanol over oxide-supported copper, *Journal of the American Chemical Society*, 2016, **138**, 12440-12450, doi: 10.1021/jacs.6b05791.

[14] D. Pan, F. Su, C. Liu, Z. Guo, Research progress for plastic waste management and manufacture of value-added products, *Advanced Composites and Hybrid Materials*, 2020, **3**, 443-461, doi: 10.1007/s42114-020-00190-0.

[15] S. I. Pomogailo, E. V. Shuvalova, E. I. Knerel'man, O. P. Tkachenko, E. G. Chepaikin, D. A. Pomogailo, L. M. Kustov, A Pd-Cu nanosized catalyst supported on γ-Al_2O_3 for liquid-phase nitrobenzene hydrogenation, *Catalysis Letters*, 2025, **155**, 298, doi: 10.1007/s10562-025-05136-z.

[16] M. Li, Y. Jiang, W. Chen, Y. Huang, Y. Lu, L. Xu, S. Li, Y. Wu, Z. Xia, R. Wang, S. Wang, Y. Zou, Internal lattice oxygen sites invert product selectivity in electrocatalytic alkyne hydrogenation over copper catalysts, *Nature Communications*, 2025, **16**, 3884, doi: 10.1038/s41467-025-58001-3.

[17] B. Chen, B. Hui, Y. Dong, Q. Sheng, X. Li, Q. Hao, C. Liu, Distributions of Ni in MCM-41 for the hydrogenation of N-ethylcarbazole, *Fuel*, 2022, **324**, 124405, doi: 10.1016/j.fuel.2022.124405.

[18] D. J. Moon, H.-K. Jeong, W. T. Lim, K. Seff, Structure of a cyclohexane sorption complex of partially dehydrated, fully Mn^{2+}-exchanged zeolite Y (FAU, Si/Al = 1.56), *Microporous and Mesoporous Materials*, 2018, **264**, 139-146, doi: 10.1016/j.micromeso.2018.01.016.

[19] F. Jokar, S. M. Alavi, M. Rezaei, Investigating the hydroisomerization of n-pentane using Pt supported on ZSM-5, desilicated ZSM-5, and modified ZSM-5/MCM-41, *Fuel*, 2022, **324**, 124511, doi: 10.1016/j.fuel.2022.124511.

[20] C. Zhai, H. Yin, J. Li, A. Wang, L. Shen, J. Hu, Catalytic conversion of 2, 5-dichlorotoluene over Hβ zeolite, Ag/Hβ and Cu/Hβ catalysts in N_2 or H_2 atmosphere, *Reaction Kinetics, Mechanisms and Catalysis*, 2017, **122**, 369-384, doi: 10.1007/s11144-017-1209-8.

[21] W. Wang, K. Wu, P. Liu, L. Li, Y. Yang, Y. Wang, Hydrodeoxygenation of *p*-cresol over Pt/Al_2O_3 catalyst promoted by ZrO_2, CeO_2, and CeO_2–ZrO_2, *Industrial & Engineering Chemistry Research*, 2016, **55**, 7598-7603, doi: 10.1021/acs.iecr.6b00515.

[22] J. D. C. Geovo, J. A. Torres, A. S. Giroto, F. L. Santos, J. R. C. Souza, L. S. Ribeiro, A. E. Nogueira, Effect of CuO synthesis on the activity and selectivity of MCM-41/CuO composites in the CO_2 photoreduction process, *Materials Letters*, 2024, **356**, 135608, doi: 10.1016/j.matlet.2023.135608.

[23] V. Brahmkhatri, A. Patel, An efficient green catalyst comprising 12-tungstophosphoric acid and MCM-41: synthesis characterization and diesterification of succinic acid, a potential bio-platform molecule, *Green Chemistry Letters and Reviews*, 2012, **5**, 161-171, doi: 10.1080/17518253.2011.607471.

[24] Y. Zhao, D. Chen, J. Liu, D. He, X. Cao, C. Han, J. Lu, Y. Luo, Tuning the metal-support interaction on chromium-based catalysts for catalytically eliminate methyl mercaptan: Anchored active chromium species through surface hydroxyl groups, *Chemical Engineering Journal*, 2020, **389**, 124384, doi: 10.1016/j.cej.2020.124384.

[25] H. Valdés, L. M. Molina, J. A. Alonso, Water adsorption and dissociation on gold catalysts supported on anatase-TiO_2(101), *Applied Surface Science*, 2019, **487**, 244-252, doi: 10.1016/j.apsusc.2019.04.249.

[26] R. Díaz, S. Macías, E. Cázares, Fourier transform infrared spectroscopy and atomic force microscopy studies of a SiO_2-TiO_2-zeolite matrix for a CuO-CoO catalyst prepared by a Sol–gel method, *Journal of Sol-Gel Science and Technology*, 2005, **35**, 13-20, doi: 10.1007/s10971-005-3210-3.

[27] M. Makowska-Janusik, A. Kassiba, N. Errien, A. Mehdi, Mesoporous silica functionalized by cyclam–metal groups: spectroscopic studies and numerical modeling, *Journal of Inorganic and Organometallic Polymers and Materials*, 2010, **20**, 761-773, doi: 10.1007/s10904-010-9400-7.

[28] F. Yang, H. Zhao, W. Wang, L. Wang, L. Zhang, T. Liu, J. Sheng, S. Zhu, D. He, L. Lin, J. He, R. Wang, Y. Li, Atomic origins of the strong metal–support interaction in silica supported catalysts, *Chemical Science*, 2021, **12**, 12651-12660, doi: 10.1039/d1sc03480d.

[29] R. Shu, R. Li, Y. Liu, C. Wang, P.-F. Liu, Y. Chen, Enhanced adsorption properties of bimetallic RuCo catalyst for the hydrodeoxygenation of phenolic compounds and raw lignin-oil, *Chemical Engineering Science*, 2020, **227**, 115920, doi: 10.1016/j.ces.2020.115920.

[30] Z. Roosta, A. Izadbakhsh, A. M. Sanati, S. Osfouri, Synthesis and evaluation of NiO@MCM-41 core–shell nanocomposite in the CO_2 reforming of methane, *Journal of Porous Materials*, 2018, **25**, 1135-1145, doi: 10.1007/s10934-017-0525-8.

[31] J. Su, X. Liu, H. Zhang, B. Zhao, Y. Feng, C. Wang, T. Shen, A density functional theory study of gas adsorption (NO, NO_2) on metal oxides (CuO, Ag_2O) modified $Ti_3C_2O_2$ monolayer, *Physica Status Solidi (b)*, 2024, **261**, 2300579, doi: 10.1002/pssb.202300579.

[32] J.-H. Tsai, T.-Y. Lee, H.-L. Chiang, Nitrogen adsorption and characteristics of iron, cobalt, and nickel oxides impregnated on SBA-15 mesoporous silica, *Nanomaterials*, 2023, **13**, 1015, doi:

10.3390/nano13061015.
[33] I. Ben Saïd, K. Sadouki, S. Masse, T. Coradin, L. S. Smiri, S. Fessi, Advanced Pd/$Ce_xZr(1–x)O_2$/MCM-41 catalysts for methane combustion: Effect of the zirconium and cerium loadings, *Microporous and Mesoporous Materials*, 2018, **260**, 93-101, doi: 10.1016/j.micromeso.2016.10.044.
[34] E. Binaeian, H.-A. Tayebi, A. Shokuhi Rad, S. Afrashteh, Adsorption of acid blue on synthesized polymeric nanocomposites, PPy/MCM-41 and PAni/MCM-41: Isotherm, thermodynamic and kinetic studies, *Journal of Macromolecular Science, Part A*, 2018, **55**, 269-279, doi: 10.1080/10601325.2018.1424554.
[35] C.-W. Shi, W.-Y. Wu, S. Li, X. Bian, S.-L. Zhao, M.-Y. Pei, Investigation of Y/SBA composite molecular sieves morphology control and catalytic performance for n-pentane aromatization, *Scientific Reports*, 2016, **6**, 23826, doi: 10.1038/srep23826.
[36] G. V. A. Martins, G. Berlier, C. Bisio, S. Coluccia, H. O. Pastore, L. Marchese, Quantification of Brønsted acid sites in microporous catalysts by a combined FTIR and NH_3-TPD study, *The Journal of Physical Chemistry C*, 2008, **112**, 7193-7200, doi: 10.1021/jp710613q.
[37] Z. Lv, L. Kang, X. Pan, Y. Su, H. Wang, L. Li, X. Y. Liu, A. Wang, T. Zhang, CuO_x nanopatches positioned at lewis acidic sites of TiO_2 for propylene epoxidation using molecular oxygen, *ACS Catalysis*, 2024, **14**, 10172-10180, doi: 10.1021/acscatal.4c01749.
[38] W. Yin, A. Kloekhorst, R. H. Venderbosch, M. V. Bykova, S. A. Khromova, V. A. Yakovlev, H. J. Heeres, Catalytic hydrotreatment of fast pyrolysis liquids in batch and continuous set-ups using a bimetallic Ni–Cu catalyst with a high metal content, *Catalysis Science & Technology*, 2016, **6**, 5899-5915, doi: 10.1039/c6cy00503a.
[39] S. Ali, L. Chen, F. Yuan, R. Li, T. Zhang, S. U. H. Bakhtiar, X. Leng, X. Niu, Y. Zhu, Synergistic effect between copper and cerium on the performance of Cu-$Ce_{0.5}$: $Zr_{0.5}$ (x= 0.1–0.5) oxides catalysts for selective catalytic reduction of NO with ammonia, *Applied Catalysis B: Environmental*, 2017, **210**, 223-234, doi: 10.1016/j.apcatb.2017.03.065.
[40] P. Barrio, M. Kumar, Z. Lu, J. Han, B. Xu, G. B. Hammond, Acidic co-catalysts in cationic gold catalysis, *Chemistry – A European Journal*, 2016, **22**, 16410-16414, doi: 10.1002/chem.201603478.
[41] M. A. Wahba, R. K. Khaled, V/Zn incorporated-MCM-41: synthesis, characterization and visible light photocatalytic activity for tetracycline degradation, *Journal of Inorganic and Organometallic Polymers and Materials*, 2025, **35**, 4445-4464, doi: 10.1007/s10904-024-03533-2.
[42] Y. Li, J. Wang, C. Ding, L. Ma, Y. Xue, J. Guo, S. Wang, Y. Meng, K. Zhang, P. Liu, Effect of cobalt addition on the structure and properties of Ni–MCM-41 for the partial oxidation of methane to syngas, *RSC Advances*, 2019, **9**, 25508-25517, doi: 10.1039/c9ra03534f.
[43] J. Nisar, R. Ullah, G. Ali, A. Shah, M. I. Din, Z. Hussain, R. Amin, Thermocatalytic decomposition of sesame waste biomass over Ni-co-doped MCM-41: kinetics and physicochemical properties of the bio-oil, *Energies*, 2023, **16**, 3731, doi: 10.3390/en16093731.
[44] R. K. Khaled, M. A. Wahba, M. D. Badry, M. F. Zawrah, E. A. Heikal, Highly ordered pure and indium-incorporated MCM-41 mesoporous adsorbents: synthesis, characterization and evaluation for dye removal, *Journal of Materials Science*, 2022, **57**, 4504-4527, doi: 10.1007/s10853-022-06877-7.
[45] S. Echaroj, N. Pannucharoenwong, P. Rattanadecho, C. Benjapiyaporn, J. Benjapiyaporn, Investigation of palm fibre pyrolysis over acidic catalyst for bio-fuel production, *Energy Reports*, 2021, **7**, 599-607, doi: 10.1016/j.egyr.2021.07.093.
[46] D. S. Lima, O. W. Perez-Lopez, Synthesis and properties of template-free mesoporous alumina and its application in gas phase dehydration of glycerol, *Powder Technology*, 2021, **378**, 737-745, doi: 10.1016/j.powtec.2020.10.031.
[47] Q. Cheng, Y. Tian, S. Lyu, N. Zhao, K. Ma, T. Ding, Z. Jiang, L. Wang, J. Zhang, L. Zheng, F. Gao, L. Dong, N. Tsubaki, X. Li, Confined small-sized cobalt catalysts stimulate carbon-chain growth reversely by modifying ASF law of Fischer–Tropsch synthesis, *Nature Communications*, 2018, **9**, 3250, doi: 10.1038/s41467-018-05755-8.
[48] M. Yang, J. Yu, A. Zimina, B. B. Sarma, J.-D. Grunwaldt, H. Zada, L. Wang, J. Sun, Unlocking a dual-channel pathway in CO_2 hydrogenation to methanol over single-site zirconium on amorphous silica, *Angewandte Chemie International Edition*, 2024, **63**, e202312292, doi: 10.1002/anie.202312292.
[49] L. Su, Z. Guan, Q. Li, C. Li, X. Wang, X. Li, J. Yang, Z. Zhang, Synthesis of SO_{42}−/Zr-silicalite-1 zeolite catalysts for upgrading and visbreaking of heavy oil, *Journal of Nanoparticle Research*, 2017, **19**, 305, doi: 10.1007/s11051-017-4002-8.
[50] Y.-M. Kim, J. Jae, S. Myung, B. H. Sung, J.-I. Dong, Y.-K. Park, Investigation into the lignin decomposition mechanism by analysis of the pyrolysis product of Pinus radiata, *Bioresource Technology*, 2016, **219**, 371-377, doi: 10.1016/j.biortech.2016.08.001.
[51] C. Li, C. Zhang, K. Sun, Z. Zhang, L. Zhang, S. Zhang, Q. Liu, G. Hu, S. Wang, X. Hu, Pyrolysis of saw dust with co-feeding of methanol, *Renewable Energy*, 2020, **160**, 1023-1035, doi: 10.1016/j.renene.2020.06.080.
[52] M. Nagyházi, Á. Lukács, G. Turczel, J. Hancsók, J. Valyon, A. Bényei, S. Kéki, R. Tuba, Catalytic decomposition of long-chain olefins to propylene *via* isomerization-metathesis using latent bicyclic (alkyl)(amino)carbene-ruthenium olefin

metathesis catalysts, *Angewandte Chemie International Edition*, 2022, **61**, e202204413, doi: 10.1002/anie.202204413.
[53] Y. Zheng, J. Wang, C. Liu, Y. Lu, X. Lin, W. Li, Z. Zheng, Efficient and stable Ni-Cu catalysts for *ex situ* catalytic pyrolysis vapor upgrading of oleic acid into hydrocarbon: Effect of catalyst support, process parameters and Ni-to-Cu mixed ratio, *Renewable Energy*, 2020, **154**, 797-812, doi: 10.1016/j.renene.2020.03.058.
[54] P. Gupta, S. Dwivedi, A. C. T. van Duin, S. Srinivas, A. Tanksale, Coke resistant catalyst for hydrogen production in a versatile, multi-fuel, reformer, *Journal of Catalysis*, 2021, **402**, 177-193, doi: 10.1016/j.jcat.2021.08.031.